Design, Manufacturing, Modelling, and Control of a Cable-Driven Parallel Robot for Additive Manufacturing*

Molong Duan, *Member*, IEEE, Jiaquan Feng, and Shuai Liu

2023 IEEE 19th International Conference on Automation Science and Engineering (CASE) | 979-8-3503-2069-5/23/$31.00 ©2023 IEEE | DOI: 10.1109/CASE56687.2023.10260537

***Abstract*— The cable-driven parallel robots are desirable for the manufacturing of large-scale structures due to their enhanced level of flexibility. This is particularly appealing in future construction industry additive manufacturing, where the system can be conveniently deployed at different locations with minimum setup change. This paper proposed a cable-driven parallel robot prototype design for additive manufacturing applications. The cable-driven parallel robot has 6 degrees of freedom and is thus capable of performing translational and rotational manipulation. To address the tension-induced inaccuracies in actuating the cable-driven robot, this paper presents a compensation method to consider the tension force and positioning error by modifying the trajectory and its geometrical relationships. Enhanced positioning performances and the 3D printing results are verified through experiments.**

I. Introduction

The cable driving mechanisms are increasingly popular in applications where large-scale manipulations are needed [1]. The cable-driven parallel robots (CDPR) have the advantage of maneuvering the end effector (EE) to arbitrary locations without pre-arranged guideways and gantry systems, thus significantly reducing the system setup time and cost. In addition, the parallel kinematics of CDPR ensures that errors from different degrees of freedom do not accumulate, enabling precise positioning even for large workspaces [2]. CDPRs offer further advantages, such as high payload capacity, low inertia, and the ability to move in complex trajectories [3]. Therefore, there has been a growing trend of applying the corresponding mechanisms in construction [4]–[6], large-scale telescopes [7], inventory systems [8], stadium camera systems [9], and rehabilitation [10].

Despite the convenience and flexibility of CDPR, its kinematics and dynamics are highly nonlinear, posing challenges to the conventional trajectory generation control allocations. In addition, the cable's limited stiffness may cause inaccuracies in the manipulation performance, leading to drops in accuracy. The tension of the robots may also lead to over-actuation problems [11]. At the same time, the workspace of the CDPR typically faces challenges since the EE may interfere with the driving cables [12]. Therefore, for CDPR applications, enhanced algorithms for the nonlinear manipulations of the cables are needed.

The CDPR is typically controlled from the cables using geometrical relationships. Conventional trajectory generation from the geometric relationships related is summarized in [1], [13]. However, as reported in [2], the resolution, accuracy, and disturbance rejection capabilities need to be significantly improved for practical industrial applications. Particularly in the application of additive manufacturing (AM), the accuracy requirement is higher than in the construction industry, and more delicate accuracy requirements are needed. To account for this need, Qian et al. proposed a CDPR kinematics calibration method [14] to enhance the accuracy. However, the proposed analysis and methods only apply to the conventional delta 3D printer configurations, where the end effectors' rotation is naturally constrained. The methods also do not explicitly consider the tension force and the corresponding inaccuracies, which may contribute to the inaccuracy of the manipulation.

In this paper, we designed a new CDPR for AM applications and its control and calibration methods considering tension. The contributions of the paper are:

- A new CDPR for AM that allows 6-degree-of-freedom (DOF) manipulation of the EE is designed and manufactured,
- A cable length control method that considers the tension force is established,
- An error compensation method combining the laser tracker and an inertial measurement unit (IMU) is established,
- The proposed design, control, and compensation methods have been experimentally verified.

The control and compensation methods are detailed in Section II. The detailed design and experimental verifications are in Section III, followed by the conclusion and future work in Section IV.

II. CDPR Control with Tension and Error Compensation

A. CDPR control considering the tension

The proposed CDPR control method builds on top of the definition and key results presented in [13]. Define an n DOF CDPR which is actuated with m cables. The conditions $m<n$, $m=n$, and $m>n$ correspond to the under-actuated, fully constrained, and over-actuated scenarios, respectively. For conventional 6 DOF CDPR that allows the rotation of the EE, the geometry schematics of the CDPR are

* Research was partially supported in part by the Project of Hetao Shenzhen-Hong Kong Science and Technology Innovation Cooperation Zone (HZQB-KCZYB-2020083).

M. Duan is with Hong Kong University of Science and Technology, Hong Kong SAR, China, as well as HKUST Shenzhen-Hong Kong Collaborative Innovation Research Institute, Futian, Shenzhen, China (corresponding author, phone: (852) 3469 3024; e-mail: duan@ust.hk).

J. Feng and S. Liu are with Hong Kong University of Science and Technology, Hong Kong SAR, China (e-mails: jfengax@connect.ust.hk, sliucr@connect.ust.hk).

specified as in Fig. 1.

Define an inertial frame $\mathcal{F}_0$ fixed to the ground and a body-fixed frame $\mathcal{F}_B$ attached to the center of gravity (CG) of the EE. Vectors projected in to $\mathcal{F}_B$ will be highlighted with superscript $^{(B)}$; other vectors are assumed to be projected to $\mathcal{F}_0$ by default. Assume m cables are attached to the anchoring points $\mathbf{a}_1$, $\mathbf{a}_2$, $\dots \mathbf{a}_m$, where $\mathbf{a}_j \in \mathbb{R}^3$ are their coordinates in $\mathcal{F}_0$. The corresponding m connection points on the EE are defined as $\mathbf{b}_1^{(B)}$, $\mathbf{b}_2^{(B)}$, $\dots \mathbf{b}_m^{(B)}$, where $\mathbf{b}_j^{(B)} \in \mathbb{R}^3$ are their coordinates in $\mathcal{F}_B$. Define the CG's location as $\mathbf{r}$ projected into $\mathcal{F}_0$ and the Euler angles $\boldsymbol{\vartheta} = \{\psi,\ \theta,\ \phi\}^\top$ following the ZYX rotation sequence. The vector representing the cables from the EE connection points to the anchoring points $\mathbf{l}_j$ are defined as

$$\mathbf{l}_j = \mathbf{a}_j - \mathbf{r} - \underbrace{\mathbf{R}(\boldsymbol{\vartheta})\mathbf{b}_j^{(B)}}_{\mathbf{b}_j}, \tag{1}$$

where $\mathbf{R}(\boldsymbol{\vartheta})$ is the rotation matrix satisfying

$$\mathbf{R}(\boldsymbol{\vartheta}) = \begin{bmatrix} \mathrm{c}_\theta \mathrm{c}_\phi & \mathrm{s}_\psi \mathrm{s}_\theta \mathrm{c}_\phi - \mathrm{c}_\psi \mathrm{s}_\phi & \mathrm{c}_\psi \mathrm{s}_\theta \mathrm{c}_\phi + \mathrm{s}_\psi \mathrm{s}_\phi \\ \mathrm{c}_\theta \mathrm{s}_\phi & \mathrm{s}_\psi \mathrm{s}_\theta \mathrm{s}_\phi + \mathrm{c}_\psi \mathrm{c}_\phi & \mathrm{c}_\psi \mathrm{s}_\theta \mathrm{s}_\phi - \mathrm{s}_\psi \mathrm{c}_\phi \\ -\mathrm{s}_\theta & \mathrm{s}_\psi \mathrm{c}_\theta & \mathrm{c}_\psi \mathrm{c}_\theta \end{bmatrix}, \tag{2}$$

where c_θ and s_θ are concise forms of $\cos(\theta)$ and $\sin(\theta)$. The unit directional vector is thus defined as

$$\mathbf{u}_j = \frac{\mathbf{l}_j}{L_j},\ L_j = \|\mathbf{l}_j\|_2. \tag{3}$$

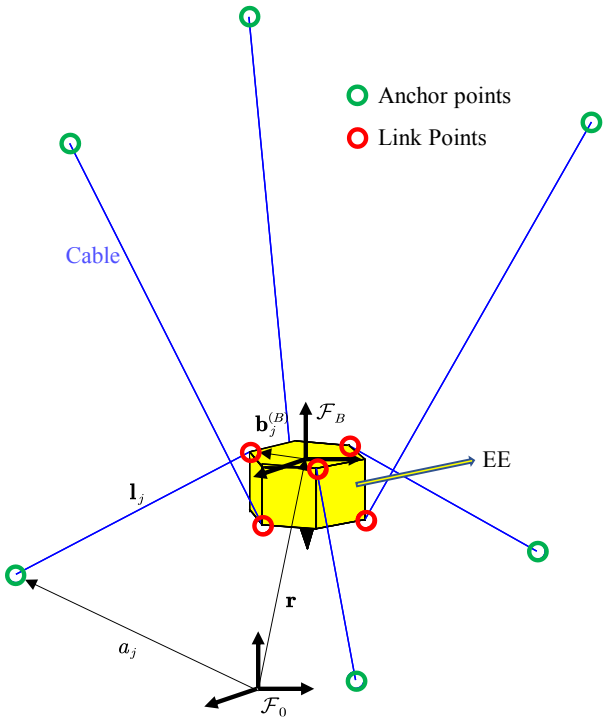

Fig. 1. Geometry schematics of CDPR.

The most straightforward control of the CDPR uses the length defined in (3) to actuate the individual motors. This method is referred to as the geometry-based method (GM) in this paper. Despite the convenience and simplicity of the GM, the method does not explicitly consider the limited stiffness of the cables. Therefore, it may lead to geometrical inaccuracies when the EE is heavy or under excessive load. This would be a severe issue when the CDPR is applied in manufacturing scenarios with external disturbances (e.g., 3D printing) or outdoor environment with gust. Therefore, this manuscript proposes to consider the stiffness and load in commanding the trajectories of the individual motors. To achieve this goal, the forces of each cable $f_1, \dots f_m$ should statically satisfy

$$\underbrace{\begin{bmatrix} \mathbf{u}_1 & \cdots & \mathbf{u}_m \\ \mathbf{b}_1 \times \mathbf{u}_1 & \cdots & \mathbf{b}_m \times \mathbf{u}_m \end{bmatrix}}_{\mathbf{A}} \underbrace{\begin{Bmatrix} f_1 \\ \vdots \\ f_m \end{Bmatrix}}_{\mathbf{f}} + \underbrace{\begin{Bmatrix} \mathbf{f}_{ext} \\ \boldsymbol{\tau}_{ext} \end{Bmatrix}}_{\mathbf{w}} = \mathbf{0}, \tag{4}$$

where $\mathbf{f}_{ext}$ and $\boldsymbol{\tau}_{ext}$ are the external force and torque applied to the CG, projected to $\mathcal{F}_0$. To account for the elastic properties of the cable, tension forces are further modeled in (4). The length of the cable without tension is defined to be L_{i0}. Assume linear elasticity, the deformation of the cables is shown in Fig. 2. Thus, the tension force vector is expressed as

$$\mathbf{f} = \mathbf{K}(\mathbf{L} - \mathbf{L}_0), \tag{5}$$

where $\mathbf{K} = \mathrm{diag}\{k_1,\ k_2, \cdots, k_m\}$ is a diagonal stiffness matrix,

$$\mathbf{L} = \{L_1, \cdots, L_m\},\ \mathbf{L}_0 = \{L_{10}, \cdots, L_{m0}\}. \tag{6}$$

Note that if a particular entry $T_i < 0$ indicates that the cable is in a slack condition, which is undesirable for the CDPR. In practical configurations, all the geometry-related variables (e.g., $\mathbf{u}_i$ and $\mathbf{b}_i$ in (4)) should connect to the cable length with tension $\mathbf{L}$, while the motor signal should connect to the cable length under the slack condition $\mathbf{L}_0$.

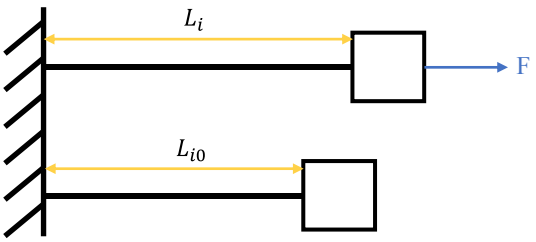

Fig. 2. Illustration of the cables with and without tension.

To acquire the proper motor reference command $\mathbf{L}_0$ that accounts for tension, combine the location and orientation of the end effector as

$$\mathbf{p} = \{\mathbf{r}^\top, \boldsymbol{\vartheta}^\top\}^\top. \tag{7}$$

The static balance equation (4) is thus converted to

$$\mathbf{A}(\mathbf{p})\mathbf{K}(\mathbf{L}(\mathbf{p}) - \mathbf{L}_0(\mathbf{p})) + \mathbf{w} = \mathbf{0}. \tag{8}$$

Given an arbitrary spatial location and orientation $\mathbf{p}$, the geometrical length $\mathbf{L}(\mathbf{p})$ and effectiveness matrix $\mathbf{A}(\mathbf{p})$ is fixed. Therefore, motor reference command $\mathbf{L}_0$, when the system is fully constrained (i.e., $m = n$), is solved as

$$\mathbf{L}_0(\mathbf{p}) = \mathbf{L}(\mathbf{p}) + (\mathbf{A}(\mathbf{p})\mathbf{K})^{-1}\mathbf{w}. \tag{9}$$

For under-actuated or over-actuated systems (i.e., $m \neq n$), the motor reference command $\mathbf{L}_0$ can be solved under a quadratic programming setup. This method of modifying the motor reference command based on the stiffness of the cable is referred to as the tension-considering method (TCM) in this paper.

B. CDPR control with error compensation

As a common challenge in the cable-driven parallel robot, the geometric motion error significantly degrades the achievable positioning accuracy. The error map is measured and further fed into the geometrical relationship considering tension in (9) to improve the positioning accuracy.

The error map is generated with the measurement from a laser tracker and its spherically mounted retroreflectors (SMR), as illustrated in Fig. 3. The SMR is attached to the nozzle and moves with it during the process. Note that the laser tracker typically only measures the XYZ locations of SMR. Therefore, to get the accurate location of the nozzle (most crucial for the printing), it is desirable to transform the laser tracker measurement with the angle measurement from an IMU device. Assume the IMU provides the Euler angles of the EE $\boldsymbol{\vartheta} = \{\psi, \theta, \phi\}^\top$ following the ZYX rotation sequence. The nozzle location in the global coordinate system $\mathbf{r}_n$ is given by

$$\mathbf{r}_n = \mathbf{r}_s + \mathbf{R}(\boldsymbol{\vartheta})\mathbf{h}^{(B)}, \tag{10}$$

where $\mathbf{r}_s$ is the location of the center of SMR relative to the global coordinate system measured by the laser tracker, and $\mathbf{h}^{(B)}$ is the distance vector from the SMR to the nozzle in the body-fixed frame $\mathcal{F}_B$.

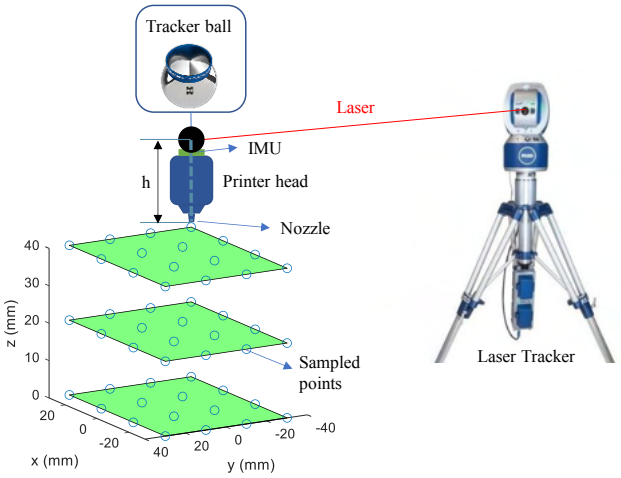

Fig. 3. Position error map measurement with laser tracker schematics.

The compensation is built on an error map from the coordinates as sampled in Fig. 3. The detailed error compensation process is shown in Fig. 4. First, the coordinates of the points $\mathbf{r}_d$ to be measured are designed, covering the workspace of the EE. Then G-code is generated, maneuvering the EE to the designated locations, and the nozzle location $\mathbf{r}_m$ is measured using the laser tracker. The corresponding positioning error at this point is given by

$$\mathbf{e} = \mathbf{r}_m - \mathbf{r}_d, \tag{11}$$

then, the error is compared with a given tolerance ϵ_0. If the error exceeds the tolerance, the error compensation is needed. After visiting a sequence of points and acquiring its error, the error map of the workspace is generated. This error map is further interpolated for trajectory compensation in future motion trajectory generated from the G-code. In the G-code, the destination position is reset from $\mathbf{r}_d$ to $\mathbf{r}_d - \mathbf{e}$. While keeping the orientation unchanged, the position and orientation vector is recursively defined as

$$\begin{aligned} \mathbf{p}_{r,k} &= \{\mathbf{r}_{d,k}{}^\top, \boldsymbol{\vartheta}^\top\}^\top, \\ \mathbf{r}_{d,k} &= \mathbf{r}_{d,k-1} - \mathbf{e}_{k-1}, \end{aligned} \tag{12}$$

where $\mathbf{r}_{d,k}$ and $\mathbf{p}_{r,k}$ represent the compensated position and the combination of position and orientation vector after k iterations, respectively; $\mathbf{e}_k$ is the compensation error vector measured in the kth iteration. The initial condition satisfies $\mathbf{r}_{d,0} = \mathbf{r}_d$. After kth iteration, the cable reference command is generated with $\mathbf{p}_{r,k}$ representing $\mathbf{p}$ in (9). The iteration ends when $\|\mathbf{e}_k\| \leq \epsilon_0$. Specifically, the method of changing the motor reference command based on the cable stiffness and the error compensation is referred to as the tension-considering method with compensation (TCMC) in this paper.

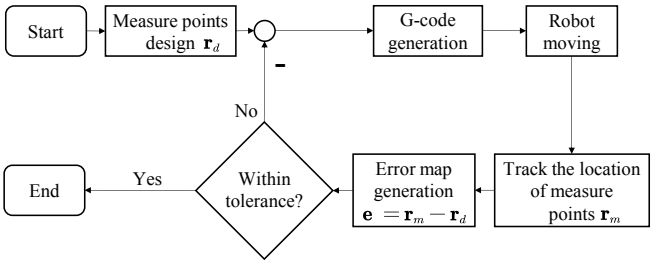

Fig. 4. The error map generation and compensation process.

III. Experimental Verification of the Setup

A. Cable-driven parallel robot design and prototype for additive manufacturing

The CDPR has two primary sections, an outer frame featuring a cable actuation system, and a central EE housing the printing head and essential cooling fans, as shown in Fig. 5. The outer frame consists of six identical vertical columns (shown in Fig. 6(a)) and two hexagonal rings to simplify the manufacturing process. This design is selected instead of another commonly seen spool design due to its benefit of cable alignment and enhanced actuation accuracy. On the other hand, the linear screw drive has several advantages over the spool design. The linear screw drive design eliminates the need for the motor to withstand the torque the spool provides. Additionally, the linear screw drive is simpler and does not require complex mechanisms to align the cable. The cables released from the linear screw drive go through a pulley to redirect toward the EE. In this way, the possible drifting or inconsistency in anchoring in the spool design is minimized.

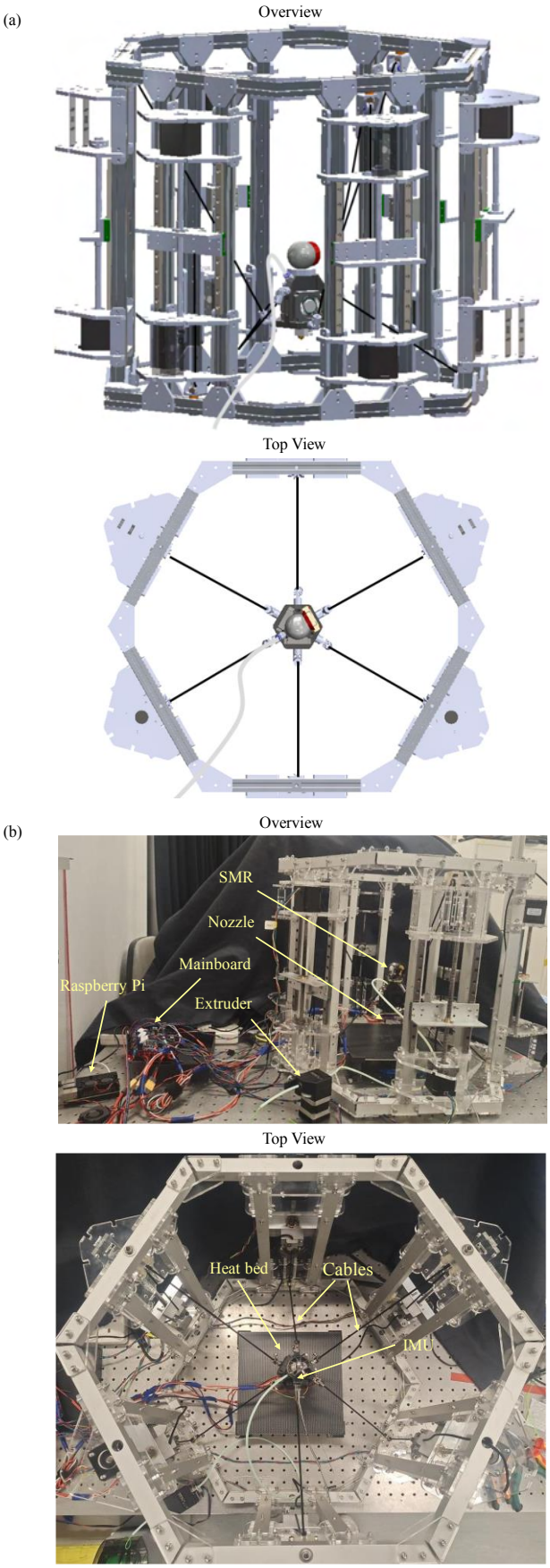

Fig. 5. Cable-driven robot (a) design and (b) prototype for additive manufacturing.

The outer frame is manufactured with high-strength aluminum stocks. The EE is connected to the outer frame using six individual cables. Six cables with a diameter equal to 3.0 mm are used; their elastic stiffness is 1.46 kN. The cables are connected to the EE with universal joints to avoid undesirable twisting. Additionally, the EE is designed to accommodate various measurement instruments, such as the inertial measurement unit (IMU) and SMR from the FARO Vantage E6 max, which is presented in Fig. 6(b). This integration design allowed for precise orientation and position measurement during the printing process, enabling further calibration of the EE's motion.

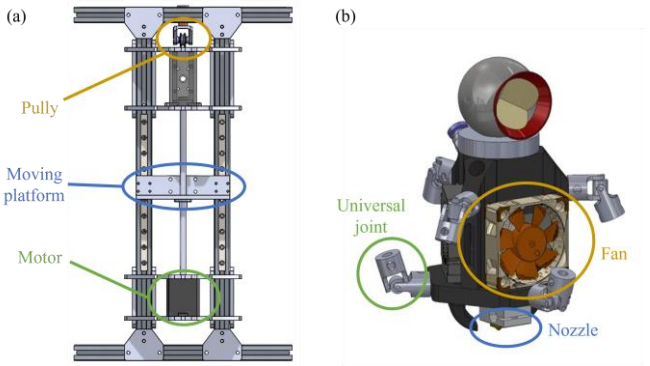

Fig. 6. (a) Cable controlling system and (b) the end effector.

The motion control hardware system, as shown in Fig. 7, is an open-loop control that starts with the generation of G-code. Once the G-code is input to the system, the open-source 3D printer control firmware Klipper running on the Raspberry Pi with the OctoPi operation system translates the G-code into internal commands for kinematics calculation and then sends out the MCU commands to control the relative actuators. Additionally, the Octoprint interface can be used to monitor and remotely control the motion of the robot. In this control system, seven stepper motors are needed to be controlled, including six stepper motors for motion control of the EE and one stepper motor for extruding the filament. For this reason, the main board BigTreeTech Octopus supporting up to eight stepper drivers, is chosen to meet the needs. The TMC 2209 motor drivers are selected for their ability to improve the accuracy of motor control and reduce noise during motion.

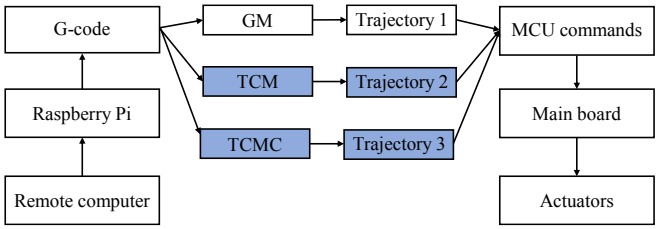

Fig. 7. Motion control diagram.

The realization of various control methods listed in (3), (9), and (12) relies on the modification of the Klipper kinematics calculation module, introducing additional parameters (e.g., stiffness) and input (error compensation map) to the original formulations.

B. *Positioning error comparison*

The positioning error of the CDPR with the GM and TCM are shown in Fig. 8 and Fig. 9, respectively, where the error map slices at $z = 0,\ 20,\ 40$ mm are presented. In both error maps, the positioning error in the x direction increases with x coordinates. A similar trend is observed with the y axis. It is also observed that the error of the z axis is relatively small compared to the x and y axis. This is a desirable feature for additive manufacturing applications with layer-by-layer printing.

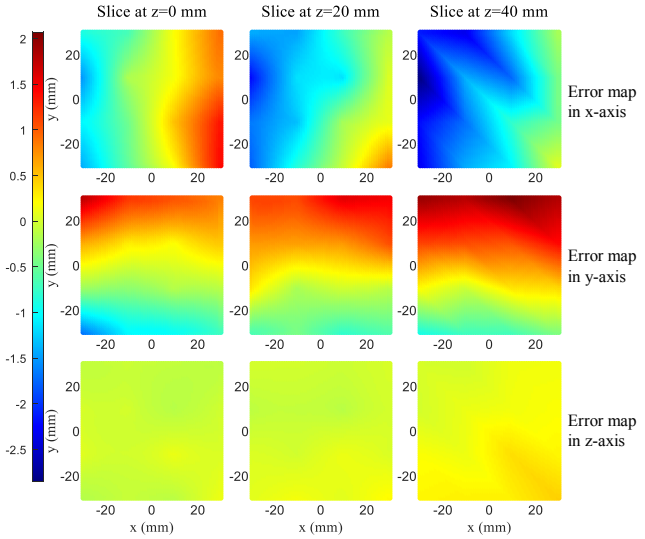

Fig. 8. Positioning error of GM (original).

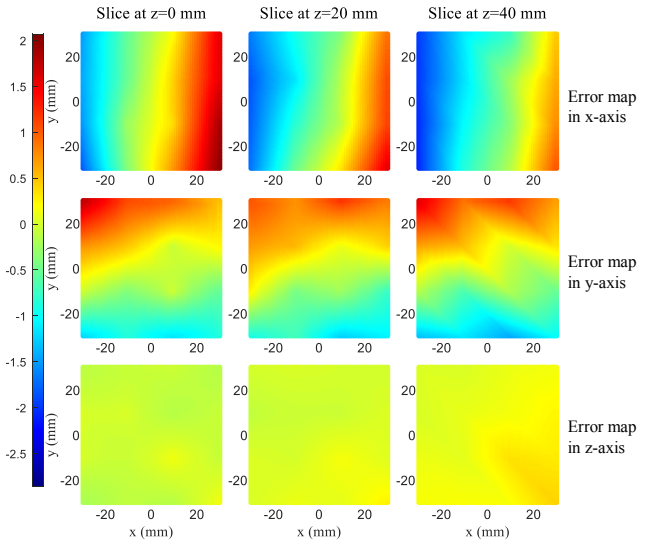

Fig. 9. Positioning error of TCM.

The maximum error of GM error is 2.8560 mm, and the maximum error of TCM error is 2.0553 mm. The error of TCM is smaller than that of GM. Then the error compensation is deployed on TCM. The error map of TCMC is shown in Fig. 10. The maximum error after compensation reaches 0.5545 mm, which is 26.98% of the maximum error of that before compensation, showing that the error is significantly decreased. The detailed numbers are shown in Table 1.

Table 1. Positioning error of different methods

	GM	TCM	TCMC
Max error [mm]	2.8560	2.0553	0.5545
RMS error [mm]	1.2589	1.1922	0.2391

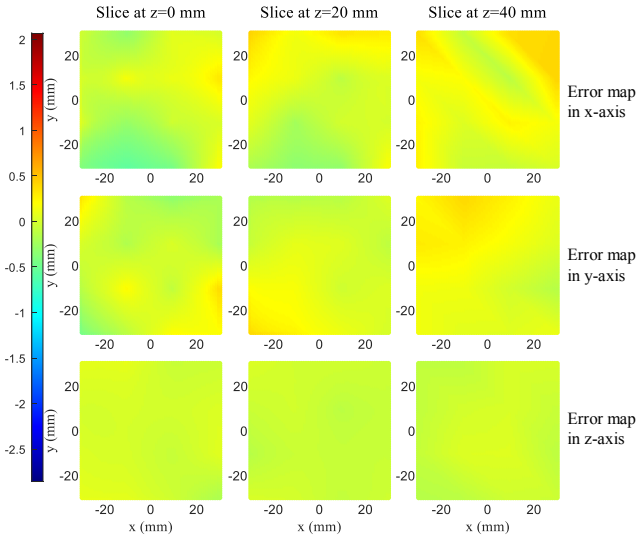

Fig. 10. Positioning error of TCMC.

C. *Printing results with different methods*

The CAD model of the red sundial (a well-known icon of the Hong Kong University of Science and Technology) is shown in Fig. 11 (a). And the printing results of GM, TCM, and TCMC are shown in Fig. 11 (b), (c), and (d), respectively. Fig. 11 (d) shows a more accurate shape and fewer burrs, which indicates better printing accuracy of TCMC.

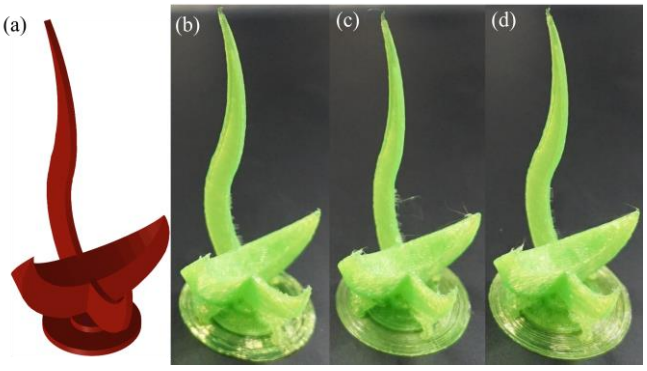

Fig. 11. (a) CAD figure and printing results with (b) GM, (c) TCM, and (d) TCMC.

IV. Conclusion and Future Work

In this paper, a 6-DOF cable-driven parallel robot was designed and manufactured for additive manufacturing. The end effector can be freely maneuvered with transitional and rotational motion. To account for the cable tension and due to gravity and other external force, a tension-considering method (TCM) and a tension-considering method with compensation (TCMC) are developed based on the modification of the kinematic relationship of the conventional

geometry-based method (GM). Enhanced positioning accuracy and printing performances have been observed.

Future work on the methods includes the consideration of other forces besides gravity, optimal disturbance rejection control, other redundant actuation schemes, and the error compensation concerning the error in the orientation to complete the accurate control of EE's orientation.

ACKNOWLEDGMENT

The authors would thank Mr. Cheuk Hei Lam, Chin Fung Chan, King Hei (Adrian) Ho, and Kin Ho (Leo) Liao for their preliminary investigation into the CDPR setup.

REFERENCES

[1] S. Qian, B. Zi, W. W. Shang, and Q. S. Xu, "A review on cable-driven parallel robots," *Chinese J. Mech. Eng. (English Ed.*, vol. 31, no. 4, 2018, doi: 10.1186/s10033-018-0267-9.

[2] J.-B. Izard *et al.*, "Large-scale 3D printing with cable-driven parallel robots," *Constr. Robot.*, vol. 1, no. 1–4, pp. 69–76, 2017, doi: 10.1007/s41693-017-0008-0.

[3] X. Tang, "An overview of the development for cable-driven parallel manipulator," *Adv. Mech. Eng.*, vol. 2014, 2014, doi: 10.1155/2014/823028.

[4] H. Mattern, T. Bruckmann, A. Spengler, and M. Konig, "Simulation of automated construction using wire robots," in *2016 Winter Simulation Conference (WSC)*, Dec. 2016, pp. 3302–3313, doi: 10.1109/WSC.2016.7822361.

[5] T. P. Tho and N. T. Thinh, "Using a cable-driven parallel robot with applications in 3d concrete printing," *Appl. Sci.*, vol. 11, no. 2, pp. 1–24, 2021, doi: 10.3390/app11020563.

[6] T. Bruckmann and R. Boumann, "Simulation and optimization of automated masonry construction using cable robots," *Adv. Eng. Informatics*, vol. 50, no. April, p. 101388, 2021, doi: 10.1016/j.aei.2021.101388.

[7] R. Nan *et al.*, "The five-hundred-meter aperture spherical radio telescope (FAST) project," *Int. J. Mod. Phys. D*, vol. 20, no. 06, pp. 989–1024, 2011.

[8] B. Salah, O. Janeh, B. Noche, T. Bruckmann, and S. Darmoul, "Design and simulation based validation of the control architecture of a stacker crane based on an innovative wire-driven robot," *Robot. Comput. Integr. Manuf.*, vol. 44, pp. 117–128, 2017, doi: 10.1016/j.rcim.2016.08.010.

[9] Y. Su, Y. Qiu, P. Liu, J. Tian, Q. Wang, and X. Wang, "Dynamic Modeling, Workspace Analysis and Multi-Objective Structural Optimization of the Large-Span High-Speed Cable-Driven Parallel Camera Robot," *Machines*, vol. 10, no. 7, 2022, doi: 10.3390/machines10070565.

[10] I. Ben Hamida, M. A. Laribi, A. Mlika, L. Romdhane, S. Zeghloul, and G. Carbone, "Multi-Objective optimal design of a cable driven parallel robot for rehabilitation tasks," *Mech. Mach. Theory*, vol. 156, p. 104141, 2021, doi: 10.1016/j.mechmachtheory.2020.104141.

[11] J. A. Saglia, N. G. Tsagarakis, J. S. Dai, and D. G. Caldwell, "A high performance 2-dof over-actuated parallel mechanism for ankle rehabilitation," in *2009 IEEE International Conference on Robotics and Automation*, May 2009, pp. 2180–2186, doi: 10.1109/ROBOT.2009.5152604.

[12] J. Jung, "Workspace and Stiffness Analysis of 3D Printing Cable-Driven Parallel Robot with a Retractable Beam-Type End-Effector," *Robotics*, vol. 9, no. 3, p. 65, Aug. 2020, doi: 10.3390/robotics9030065.

[13] A. Pott, *Cable-driven parallel robots: Theory and application*, vol. 120. 2018.

[14] S. Qian, K. Bao, B. Zi, and N. Wang, "Kinematic calibration of a cable-driven parallel robot for 3D printing," *Sensors (Switzerland)*, vol. 18, no. 9, 2018, doi: 10.3390/s18092898.